Non-rigid surface proximity registration of CT images considering the influence of pleural thickenings

Peter Faltin[a], Kraisorn Chaisaowong[a,b], Thomas Kraus[c], Til Aach[a]

[a]Institute of Imaging and Computer Vision, RWTH Aachen University, Germany;
[b]King Mongkut's University of Technology North Bangkok, Thailand;
[c]Institute and Out-patient Clinic of Occupational Medicine, UK Aachen, Germany

ABSTRACT

Given two CT thorax images from the same patient taken at two different points in time, a detailed follow-up assessment of pleural thickenings and their growth requires a registration of the regarded image regions. While the spatio-temporal matching of thickenings could be achieved by a rigid registration, the direct visual comparison or the combination of thickening segmentations from different points in time require a more precise registration. We present a new method which provides a non-rigid registration of the 3D image data in the region close to the lung surface, where pleural thickenings are located. A B-spline based approach is used to compensate the non-rigid deformations of the lungs. The control-grid for the B-splines is determined using a non-iterative method, which requires matched feature points from the registered image pair. However, current non-rigid registration methods compensate all changes of the lung surface. This is in our case explicitly undesired for changes caused by pleural thickenings. Therefore, our approach takes the thickenings into account by choosing feature points not directly located on the lung surface. The number of feature points is reduced and only strong features are kept for a 3D block matching.

Keywords: non-rigid registration, free-form deformations, B-spline, convex hull, aperture problem

1. INTRODUCTION

Asbestos is known to be a human carcinogen. Its fibres can enter the lung by inhaling. They have a long persistence and can cause pleural thickenings and eventually pleural mesothelioma. An essential condition for a treatment that delays the mortality is the early detection of potential tumours. For that reason high risk patients undergo a medical examination, which includes 3D CT imaging. The manual investigation of this image data is usually performed slice-wise. One CT thorax data set contains approximately 700 slices and the screening is very time consuming and subject to strong inter- and intra-reader variation[1]. To support the physician as well as to extract and measure the thickenings a fully automatic procedure was developed[2].

For a visual comparison or a combination of segmentation information from different points in time, a non-rigid registration is required. Loeckx et al.[3] present a method which uses conditional mutual information and is based on an approach of Rueckert et al.[4]. Feature based approaches from Chui et al.[5] and Kwon et al.[6] decrease the computation time significantly. However, they do not consider the thickening growth, which might be inadvertently compensated by the registration. Our feature based method takes the thickenings into account and preserves their shape in the registered image.

2. METHODS

In this paper the image $\boldsymbol{G}_1$ is registered to the image $\boldsymbol{G}_2$. Both images are taken from the same patient at two different points in time and consist of the voxels $G_1(\boldsymbol{r})$ and $G_2(\boldsymbol{r})$, where $\boldsymbol{r} = (x, y, z)^T \in \boldsymbol{R}$ are the image coordinates. In addition to the image data our approach requires the associated lung masks $\boldsymbol{R}_{\mathrm{L},1} \subset \boldsymbol{R}$ and $\boldsymbol{R}_{\mathrm{L},2} \subset \boldsymbol{R}$, which are extracted using a two-step supervised range-constrained Otsu thresholding.[7]

Further author information: (Send correspondence to P. Faltin)
P. Faltin: E-mail: peter.faltin@lfb.rwth-aachen.de, Telephone: +49 (241) 80 27865

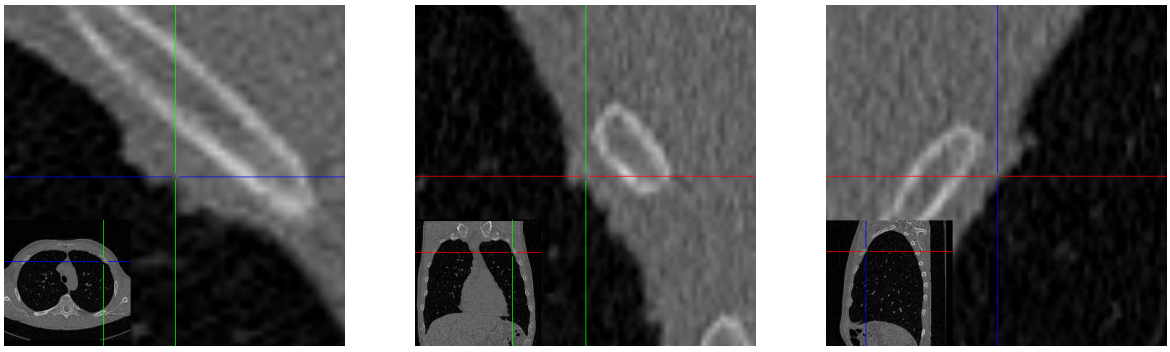

(a) Transverse plane. (b) Coronal plane. (c) Sagittal plane.

Figure 1. A pleural thickening shown in different planes

2.1 Rigid Registration

The image $\boldsymbol{G}_1$ is rigidly registered to match the image $\boldsymbol{G}_2$ using a Markov-Gibbs random fields based approach[8]. An offline training step is used to determine the Gibbs potentials adapted to lung tissue. Then the Gibbs energy is calculated using the image volumes covered by the registered lung masks from the other point in time. Maximizing this energy results in the final rigid transformation $\boldsymbol{T}_{\mathrm{r}}(\boldsymbol{r})$, and hence in the image and lung mask

$$\boldsymbol{G}_{\mathrm{r}} = \boldsymbol{G}_1(\boldsymbol{T}_{\mathrm{r}}(\boldsymbol{r})), \boldsymbol{R}_{\mathrm{L,r}} = \boldsymbol{T}_{\mathrm{r}}(\boldsymbol{R}_{\mathrm{L},1}). \tag{1}$$

2.2 Non-rigid Registration

The position of a point $\boldsymbol{r}$ is calculated using free-form deformations[9]. A grid of $N_x \times N_y \times N_z$ control points $\Phi_{\mu,\nu,\xi}$, with $(\mu,\nu,\xi) \in \mathbb{N}$, $1 \leqslant \mu \leqslant N_x, 1 \leqslant \nu \leqslant N_y, 1 \leqslant \xi \leqslant N_z$ and the spacings δ_x, δ_y and δ_z, is used to determine the transformation

$$\boldsymbol{T}_{\mathrm{nr}}(\boldsymbol{r}) = \sum_{l=0}^{3}\sum_{m=0}^{3}\sum_{n=0}^{3} B_l(u)B_m(v)B_n(w)\Phi_{i+l,j+m,k+n}, \tag{2}$$

with $i = \left\lfloor \frac{x}{\delta_x} \right\rfloor + 1$, $j = \left\lfloor \frac{y}{\delta_y} \right\rfloor + 1$, $k = \left\lfloor \frac{z}{\delta_z} \right\rfloor + 1$, $u = \frac{x}{N_x} - \left\lfloor \frac{x}{\delta_x} \right\rfloor$, $v = \frac{y}{N_y} - \left\lfloor \frac{y}{\delta_y} \right\rfloor$, $w = \frac{z}{N_z} - \left\lfloor \frac{z}{\delta_z} \right\rfloor$. $B_c(s)$ is the c-th basis function of the cubic and uniform B-spline

$$\begin{aligned} B_0(s) &= \frac{(1-s)^3}{6}, \\ B_1(s) &= \frac{3s^3 - 6s^2 + 4}{6}, \\ B_2(s) &= \frac{-3s^3 + 3s^2 + 3s + 1}{6}, \\ B_3(s) &= \frac{s^3}{6}. \end{aligned} \tag{3}$$

This transformation $\boldsymbol{T}_{\mathrm{nr}}(\boldsymbol{r})$ is used to interpolate the non-rigidly registered image

$$\boldsymbol{G}_{\mathrm{nr}} = \boldsymbol{G}_{\mathrm{r}}(\boldsymbol{T}_{\mathrm{nr}}(\boldsymbol{r})). \tag{4}$$

Using this model only the positions of the control points $\Phi_{\mu,\nu,\xi}$ have to be determined. The transformations of all other voxels are interpolated using the cubic B-splines according to eq. 2. In current methods the transformed points $\Phi_{\mu,\nu,\xi}$ are determined using an iterative minimization of intensity based error metrics[4,3] or using feature points[5,6]. Our approach uses feature points close to the lung surface which are not affected by thickenings (see sect. 2.3). Using these points and their translation between the images $\boldsymbol{G}_r$ and $\boldsymbol{G}_2$ the control points are calculated using the algorithm from Lee et al[10].

2.3 Calculation of Feature Points and the Corresponding Translation

We eliminate the influence of the thickenings on the lung surface by constructing a slice-wise convex hull[2] separately for the left and right lung. The discrete set of points is given by

$$\boldsymbol{R}_{\mathrm{c}} = \bigcup_{\tilde{z}} \left\{ \sum_{\boldsymbol{r}\in\boldsymbol{R}} a_r \cdot \boldsymbol{r} \;:\; \sum_{\boldsymbol{r}\in\boldsymbol{R}} a_r = 1;\; a_r \geq 0;\; r = (x, y, \tilde{z}) \in \mathbb{Z}^3 \right\}. \tag{5}$$

The healthy lung border is not available from the CT images and cannot be easily estimated. Therefore we use the convex hull to model a virtual lung boundary not influenced by the thickenings. It is calculated for the lung masks $\boldsymbol{R}_{\mathrm{L,r}}$ and $\boldsymbol{R}_{\mathrm{L},2}$. The convex hull belonging to the rigidly registered lung image $\boldsymbol{G}_{\mathrm{r}}$ is denoted as $\boldsymbol{r}_{\mathrm{c,r}} \in \boldsymbol{R}_{\mathrm{c,r}}$, while the convex hull belonging to the lung image taken at the second point in time is denoted as $\boldsymbol{r}_{\mathrm{c},2} \in \boldsymbol{R}_{\mathrm{c},2}$. The surfaces are described by a discrete set of points. For the rigidly registered lung, the surface is given by $\partial\boldsymbol{r}_{\mathrm{c,r}} \in \partial\boldsymbol{R}_{\mathrm{c,r}} \subset \boldsymbol{R}_{\mathrm{c,r}}$ and for the second points in time by $\partial\boldsymbol{r}_{\mathrm{c},2} \in \partial\boldsymbol{R}_{\mathrm{c},2} \subset \boldsymbol{R}_{\mathrm{c},2}$. A comparison of the convex hull surface $\partial\boldsymbol{r}_{\mathrm{c},2}$ to the actual lung surface $\partial\boldsymbol{r}_2 \subset \boldsymbol{R}_{\mathrm{L},2}$ is shown in fig. 2. Especially in the red circled thickening regions, the convex surface (yellow) differs from the actual surface (green). The deformation of the lung surface

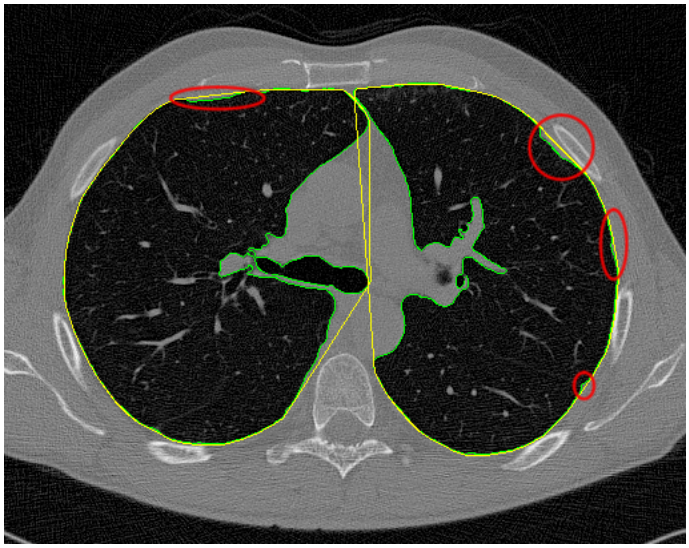

Figure 2. Comparing the convex hull (yellow) with the detected lung contour (green) in one slice for thickenings (red circles).

can be described by a translation vector $\boldsymbol{t}$ from each point $\partial\boldsymbol{r}_{\mathrm{c,r}}$ to its matching point on the surface $\partial\boldsymbol{R}_{\mathrm{c},2}$. In this paper we use 3D block matching to extract these vectors. The low density of visible structures close to the lung surface requires large blocks to include useful image information. This leads to a huge computational expense. Therefore only a very limited number of positions can be compared in a reasonable time. Translations orthogonal to the surface are automatically considered by mapping the surface voxels $\partial\boldsymbol{R}_{\mathrm{c,r}} \rightarrow \partial\boldsymbol{R}_{\mathrm{c},2}$. However translations along the surface can only be detected by matching structures orthogonal to the lung surface. This matching problem is known as the aperture problem. A visualization of the 2D case is shown in fig. 3, where one of the two sample points in G_r cannot unambiguously matched to a point in G_2, using block matching. To find surface points $\partial\boldsymbol{r}_{\mathrm{c,r}}$ containing orthogonal structures in their surrounding, the variation in each 3D block of the image is calculated separately for each dimension. This can be realized by applying a moving average on the absolute derivatives of the image. To suppress the effect of noise, the image is filtered with a discrete Gaussian kernel $\boldsymbol{L}$. The average variations in alls directions for a block size of N^3 are given by

$$\boldsymbol{V} = \frac{1}{N^3} \left(\left| \frac{\partial \boldsymbol{G}_{\mathrm{nr}} * \boldsymbol{L}}{\partial x} \right| * \boldsymbol{H}, \left| \frac{\partial \boldsymbol{G}_{\mathrm{nr}} * \boldsymbol{L}}{\partial y} \right| * \boldsymbol{H}, \left| \frac{\partial \boldsymbol{G}_{\mathrm{nr}} * \boldsymbol{L}}{\partial z} \right| * \boldsymbol{H}, \right)^T, \tag{6}$$

with the moving average $\boldsymbol{H}(i, j, k) = 1, \forall i, j, k \in \{1, \cdots, N\}$. The variation of a single surface point is denoted by $\boldsymbol{v} \in \boldsymbol{V}$. A lung surface with a mapping of $\boldsymbol{V}$ to RGB, is shown in fig. 5(a). The red dots on the upper right

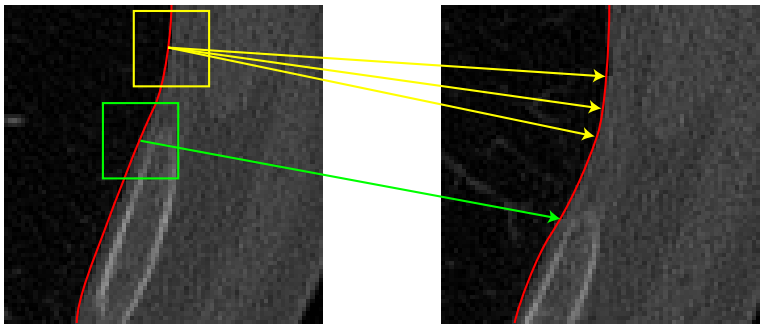

Figure 3. Aperture problem for the yellow block at the first point in time which can only be ambiguously matched to a location at the second point in time, while the green block contains enough structure to be unambiguously matched.

lung (left in the image), e.g., are caused by calcifications close to the lung surface. The normal of each point $\partial \boldsymbol{r}_{\mathrm{c,r}}$ on the discrete surface can be efficiently calculated using the method of Thürmer et al.[11]. The normals are calculated by a weighted sum of all voxels contained in the lung mask $\boldsymbol{R}_{\mathrm{c,r}}$. The weights are determined by their relative position $(i,j,k)^T$ in the neighbourhood. A normal is given by

$$\partial \boldsymbol{r}_{\mathrm{c,r}}^{\perp} = \begin{pmatrix} \sum_{i,j,k=-M, i\neq 0 \vee j\neq 0 \vee k\neq 0 \vee}^{M} \frac{\sigma \cdot i}{(i^2+j^2+k^2)^{1.5}} \\ \sum_{i,j,k=-M, i\neq 0 \vee j\neq 0 \vee k\neq 0 \vee}^{M} \frac{\sigma \cdot j}{(i^2+j^2+k^2)^{1.5}} \\ \sum_{i,j,k=-M, i\neq 0 \vee j\neq 0 \vee k\neq 0 \vee}^{M} \frac{\sigma \cdot k}{(i^2+j^2+k^2)^{1.5}} \end{pmatrix}, \tag{7}$$

with

$$\sigma = \begin{cases} 1 & (\partial \boldsymbol{r}_{\mathrm{c,r}} + (i,j,k)^T) \in \boldsymbol{R}_{\mathrm{c,r}} \\ 0 & \text{else} \end{cases}. \tag{8}$$

The information used for this calculation is shown in fig. 4 and the resulting normals with a mapping of $\partial \boldsymbol{r}_{\mathrm{c,r}}^{\perp}$ to RGB is shown in fig. 5(b). The inner product $\boldsymbol{v}^T(\partial \boldsymbol{r}_{\mathrm{c,r}}) \cdot \partial \boldsymbol{r}_{\mathrm{c,r}}^{\perp}$ is the projection of the variation in the direction

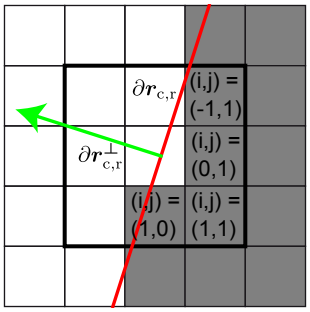

Figure 4. 2D visualization of normal (green) from discrete surface (given by the gray pixels). It is calculated from the pixel values and their positions in the 3x3 neighbourhood (represented by the bold square).

of the surface normal. The normalized absolute value of this product $|(\boldsymbol{v}^T(\partial \boldsymbol{r}_{\mathrm{c,r}}) \cdot \partial \boldsymbol{r}_{\mathrm{c,r}}^{\perp})/(\|\boldsymbol{v}(\partial \boldsymbol{r}_{\mathrm{c,r}})\|_2 \cdot \|\partial \boldsymbol{r}_{\mathrm{c,r}}^{\perp}\|_2)|$ is between 0 and 1. It is 1, when there is no structure orthogonal to the lung surface and 0 if all of the structure is orthogonal to the surface. Subtracting this value from 1 inverts the statement. Multiplying by the norm of the variation leads to

$$q = \left(1 - \left| \frac{\boldsymbol{v}(\partial \boldsymbol{r}_{\mathrm{c,r}}) \cdot \partial \boldsymbol{r}_{\mathrm{c,r}}^{\perp}}{\|\boldsymbol{v}(\partial \boldsymbol{r}_{\mathrm{c,r}})\|_2 \cdot \left\|\partial \boldsymbol{r}_{\mathrm{c,r}}^{\perp}\right\|_2} \right| \right) \cdot \|\boldsymbol{v}\|_2 , \tag{9}$$

which gives a measurement about the strength of structures orthogonal to the surface. Points with a high q value do not suffer from the aperture problem and should be preferentially chosen for the block matching. In a non-maxima suppression all values of q in a certain radius around each maximum of q are discarded. The block

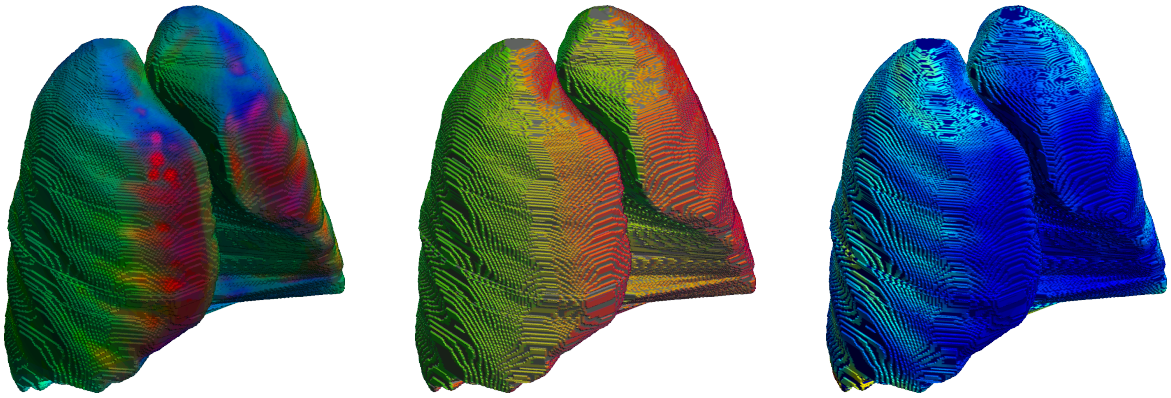

(a) Blockwise variation. (b) Surface normals. (c) Strength of structures orthogonal to the surface.

Figure 5. Steps to calculate strength of candidates used for the non-maxima suppression. (a) and (b) are color coded vectors were x,y and z direction are mapped to red, green and blue. (c) contains scalar values mapped to a color scale ranging from dark blue to yellow.

matching for a block size of N uses the summed absolute differences

$$\mathrm{SAD}(\partial \boldsymbol{r}_{\mathrm{c,r}}, \partial \boldsymbol{r}_{\mathrm{c},2}) = \sum_{i,j,k=-N}^{N} \left| (\boldsymbol{G}_{\mathrm{nr}} * \boldsymbol{L})(\partial \boldsymbol{r}_{\mathrm{c,r}} + (i,j,k)^T) - (\boldsymbol{G}_2 * \boldsymbol{L})(\partial \boldsymbol{r}_{\mathrm{c},2} + (i,j,k)^T) \right|, \tag{10}$$

as an error metric, where the discrete Gaussian kernel $\boldsymbol{L}$ is used to suppress noise. The number of examined points $\partial \boldsymbol{r}_{\mathrm{c},2}$ for each candidate is limited to a certain distance D. The translation vectors with the minimal and maximal SAD are

$$\boldsymbol{t}_{\mathrm{SAD,\ min/max}} = (\arg \quad \min_{\substack{\partial \boldsymbol{r}_{\mathrm{c},2} \in \partial \boldsymbol{R}_{\mathrm{c},2}, \\ \|\partial \boldsymbol{r}_{\mathrm{c,r}} - \partial \boldsymbol{r}_{\mathrm{c},2}\|_2 < D}} / \max \quad \mathrm{SAD}(\partial \boldsymbol{r}_{\mathrm{c,r}}, \partial \boldsymbol{r}_{\mathrm{c},2})) - \partial \boldsymbol{r}_{\mathrm{c,r}}. \tag{11}$$

Matches are discarded, when the ratio of the SAD values of the worst matching point in $\partial \boldsymbol{R}_{\mathrm{c},2}$ and the best matching point in $\partial \boldsymbol{R}_{\mathrm{c},2}$ is smaller than a certain value, i.e. the optimum is not sufficiently distinctive. In these cases the final translation vector $\boldsymbol{t}$ for a point $\partial \boldsymbol{r}_{\mathrm{c,r}}$ is replaced with the translation to its closest point in $\partial \boldsymbol{R}_{\mathrm{c},2}$

$$\boldsymbol{t} = \begin{cases} \boldsymbol{t}_{\mathrm{SAD,\ min}} & \frac{\boldsymbol{t}_{\mathrm{SAD,\ min}}}{\boldsymbol{t}_{\mathrm{SAD,\ max}}} < q \\ (\arg \min_{\partial \boldsymbol{r}_{\mathrm{c},2} \in \partial \boldsymbol{R}_{\mathrm{c},2},} \|\partial \boldsymbol{r}_{\mathrm{c,r}} - \partial \boldsymbol{r}_{\mathrm{c},2}\|_2) - \partial \boldsymbol{r}_{\mathrm{c,r}} & \text{otherwise} \end{cases}. \tag{12}$$

3. RESULTS

To evaluate the quality of the registration two different errors are measured; on the one hand the average SAD error in a surrounding $\boldsymbol{R}_{\mathrm{s},2}$ of the lung surface and on the other hand the average surface distance (ASD) of each point $\partial \boldsymbol{r}_{\mathrm{c,r}}$ to the closest point in $\partial \boldsymbol{R}_{\mathrm{c},2}$. The mask $\boldsymbol{R}_{\mathrm{s},2}$ is determined applying a dilation with a sphere of radius r as the structuring element $\boldsymbol{W}$

$$\boldsymbol{R}_{\mathrm{s},2} = \partial \boldsymbol{R}_{\mathrm{c},2} \oplus \boldsymbol{W}. \tag{13}$$

This mask $\boldsymbol{R}_{\mathrm{s},2}$ should include the image regions primarily affected by our registration method and r is therefore chosen to be equal to the grid constant. We compare the error metrics after the rigid registration with the error metrics after the non-rigid registration. The non-rigid case is evaluated using the presented method and the MATLAB implementation from Kroon (available at MATLAB central with file ID: #20057) as a reference, which is an enhanced implementation of the algorithms from Rueckert et al.[4].

While the processing for each 3D image pair (up to $512 \times 512 \times 695$ voxels) takes with the implementation from Kroon several days, our approach takes at maximum 6 minutes (run on a desktop computer: Core i5, 8GB

patient	#slices	ASD			SAD		
		rigid registration	our approach	Kroon	rigid registration	our approach	Kroon
1	695	2.098	0.633	0.829	321.3	214.9	161.1
2	397	3.741	1.911	1.470	343.5	215.3	142.4
3	57	2.566	0.829	14.100	378.1	205.3	721.1
4	411	3.433	1.442	1.660	345.5	218.4	155.1
Average		2.960	1.204	4.515	347.1	213.5	294.9

Table 1. Results for the non-rigid registration using the Kroon implementation and our approach

memory). Both implementations are MATLAB and C++ hybrid implementations. The resulting ASD is mostly smaller using our approach, while Kroon's approach performs better for the SAD. This tendency is plausible as the error metric, which performs better for each approach, is similar to its optimization criterion. The SAD value reached by the Kroon implementation is even lower than the theoretical limit for our approach, because it also deforms the thickenings, what we explicitely prevent. The failure of the Kroon implementation for patient 3 is caused by the low number of slices, which results in a strongly discontinuous image.

4. CONCLUSIONS

Our approach provides good results for the registration in the lung surface surrounding image regions, without affecting the thickening growth. The performance in these surroundings is comparable to methods with a much higher computational expense. The significantly lower runtime allows an application in end-user software for medical routine. In future development regions, where block matching fails, should be subject to a more natural interpolation instead of choosing the closest translation between the surfaces. Also the runtime has to be slightly optimized for end-user applications.

REFERENCES

[1] Ochsmann, E., Carl, T., Brand, P., Raithel, H., and Kraus, T., "Inter-reader variability in chest radiography and HRCT for the early detection of asbestos-related lung and pleural abnormalities in a cohort of 636 asbestos-exposed subjects.," *INT ARCH OCC ENV HEA* **83**, 39–46 (2010).

[2] Chaisaowong, K., Jäger, P., Vogel, S., Knepper, A., Kraus, T., and Aach, T., "Computer-assisted diagnosis for early stage pleural mesothelioma: Towards automated detection and quantitative assessment of pleural thickenings from thoracic CT images," *Methods of Information in Medicine* **46**(3), 324–331 (2007).

[3] Loeckx, D., Slagmolen, P., Maes, F., Vandermeulen, D., and Suetens, P., "Nonrigid image registration using conditional mutual information," *IEEE TMI* **29**(1), 725–737 (2007).

[4] Rueckert, D., Sonoda, L. I., Hayes, C., Hill, D. L. G., Leach, M. O., and Hawkes, D. J., "Nonrigid registration using free-form deformations: Application to breast MR images," *IEEE TMI* **18**, 712–721 (1999).

[5] Chui, H., Win, L., Schultz, R., Duncan, J. S., and Rangarajan, A., "A unified non-rigid feature registration method for brain mapping.," *Medical Image Analysis* **7**(2), 113–30 (2003).

[6] Kwon, D., Yun, I. D., Lee, K. H., and Lee, S. U., "Efficient feature-based nonrigid registration of multiphase liver CT volumes," in [*Proceedings of the BMVC*], (2008).

[7] Chaisaowong, K., Knepper, A., Kraus, T., and Aach, T., "Application of supervised range-constrained thresholding to extract lung pleura for automated detection of pleural thickenings from thoracic CT images," in [*Proceedings of the SPIE Medical Imaging*], **6514**, 65143M (2007).

[8] Faltin, P., Chaisaowong, K., Kraus, T., and Aach, T., "Markov-gibbs model based registration of CT lung images using subsampling for the follow-up assessment of pleural thickenings," in [*Proceedings of IEEE ICIP*], 2229–2232 (2011).

[9] Hsu, W. M., Hughes, J. F., and Kaufman, H., "Direct manipulation of free-form deformations," in [*Proceedings of the SIGGRAPH*], 177–184, ACM Press, New York, NY (1992).

[10] Lee, S., Wolberg, G., and Shin, S. Y., "Scattered data interpolation with multilevel B-splines," *IEEE TVCG* **3**, 228–244 (1997).

[11] Thürmer, G. and Wüthrich, C. A., "Normal computation for discrete surfaces in 3D space," *Computer Graphics Forum* **16**, 15–26 (1997).